Title

Tissue clearing techniques for three-dimensional optical imaging of intact human prostate and correlations with multi-parametric MRI

Journal

The Prostate, 81(9)

ISSN

0270-4137

Authors

Cipollari, Stefano
Jamshidi, Neema
Du, Liutao
et al.

Publication Date

2021-06-01

DOI

10.1002/pros.24129

Peer reviewed

Published in final edited form as:

Prostate. 2021 June ; 81(9): 521–529. doi:10.1002/pros.24129.

Tissue clearing techniques for three-dimensional optical imaging of intact human prostate and correlations with multi-parametric MRI

Stefano Cipollari, MD[1,2,†], **Neema Jamshidi, MD, PhD**[1,3,†], **Liutao Du, MD, PhD**[3], **Kyunghyun Sung, PhD**[3], **Danshan Huang, MD**[3], **Daniel J. Margolis, MD**[4], **Jiaoti Huang, MD, PhD**[5], **Robert E. Reiter, MD**[6], **Michael D. Kuo, MD**[*,1]

[1]Medical Artificial Intelligence Laboratory Program, The University of Hong Kong, Hong Kong SAR

[2]Department of Radiology, La Sapienza, The University of Rome, Italy

[3]Department of Radiological Sciences, University of California, Los Angeles, David Geffen School of Medicine, California

[4]Department of Radiology, Cornell University, New York

[5]Department of Pathology, Duke University School of Medicine, North Carolina

[6]Department of Urology, University of California, Los Angeles, David Geffen School of Medicine, California.

Abstract

Background—Tissue clearing technologies have enabled remarkable advancements for *in situ* characterization of tissues and exploration of the three-dimensional (3D) relationships between cells, however these studies have predominantly been performed in non-human tissues and correlative assessment with clinical imaging has yet to be explored. We sought to evaluate the feasibility of tissue clearing technologies for three-dimensional (3D) imaging of intact human prostate and the mapping of structurally and molecularly preserved pathology data with multi-parametric volumetric MR imaging (mpMRI).

[*]Correspondence should be addressed to MDK (mikedkuo@gmail.com).

[†]Co-first authorship

Authors' contributions

SC drafted the manuscript. NJ analyzed the results. LD and DH performed tissue experiments. KS performed MR measurements. JH performed histological measurements. MDK conceived of the study and its design. All authors edited the manuscript and agreed upon the final content.

The authors disclose no potential conflicts of interest.

Ethics approval and consent to participate

This study involved retrospective analysis according to an institutional review board–approved, Health Insurance Portability and Accountability Act protocol permitting evaluation of resected tissue specimens and diagnostic imaging studies.

Availability of data and materials

All data generated or analysed during this study are included in this published article and its supplementary information files.

Competing interests

The authors declare that they have no competing interests.

Methods—Whole mount prostates were processed with either hydrogel-based CLARITY or solved-based iDISCO. The samples were stained with a nuclear dye or fluorescently labeled with antibodies against AR, AMACR, or p63, and then imaged with 3D confocal microscopy. Apparent Diffusion Coefficient (ADC) and K^{trans} maps were computed from pre-operative mpMRI.

Results—Quantitative analysis of cleared normal and tumor prostate tissue volumes displayed differences in 3D tissue architecture, marker-specific cell staining, and cell densities that were significantly correlated with mpMRI measurements in this initial, pilot cohort.

Conclusions—3D imaging of human prostate volumes following tissue clearing is a feasible technique for quantitative radiology-pathology correlation analysis with mpMRI and provides an opportunity to explore functional relationships between cellular structures and cross-sectional clinical imaging.

Keywords

radiogenomics; prostate; prostate cancer; tissue clearing; CLARITY; iDISCO

Background

The noninvasive extraction of detailed structural and molecular information from intact biological systems remains a fundamental goal of medical imaging. Current methods of medical image interpretation rely on correlation between large imaging datasets encoding for both macroscopic structural, functional and dynamic information relative to large tissue volumes, and thin-section histopathology slides. Histology sections however, at an average thickness of 5 μm, are insufficient for any assessment of volumetric cell-cell interactions. Furthermore, extensive molecular phenotyping is challenging to achieve within tissue sections due to a limited ability to evaluate more than a handful of molecular markers on the same slide and to a difficulty to spatially distinguish signal in case of overlapping cells (1, 2). Thus, new methods enabling more extensive spatial mapping of medical image datasets against larger and intact tissue specimens at a structural as well as molecular level are needed and represent a critical next step in the advancement of medical imaging.

As an attempt to reduce refractive index interfaces within tissues, the main barrier to the achievement of detailed microscopic imaging of intact volumes (3-5), pioneering techniques have been developed starting in the early 1900s (6). Recently thanks to the development of technologies such as CLARITY (7) and iDISCO (8), researchers are able to extract high-resolution structural and molecular data from intact tissue volumes (7, 9-15). CLARITY combines hydrogel-based tissue embedding and lipid extraction via electrophoresis or incubation in detergent to homogenize the refractive index of the tissues, while iDISCO uses dehydration and organic solvents to remove lipids. Precise visual mapping and quantification of potentially any molecular structure across the entirety of the specimen with sub-micron resolution are also possible via the use of endogenous fluorescence or immunolabeling (7, 8).

A cornerstone of modern diagnostic medicine involves the radiology-pathology (Rad-Path) correlation (16); in the 21st Century bringing this to bear in the context of

advanced measurement capabilities in noninvasive and tissue-based measurements will be critical. Concurrently developments in clinical tomographic imaging have improved spatial resolution and improved capabilities to measure tissue and organ functional information, beyond just anatomical structures. Radiogenomics was developed to help bridge the divide between molecular phenotypes and clinical imaging phenotypes, through concordant use of omic data, histological data, clinical imaging, and clinical diagnoses/outcomes (17-25). Now, the availability of clearing techniques can potentially allow one to establish new quantitative 3D radiogenomic correlations of intact tissue volumes, preserving spatial relationships across spatial scales orders of magnitude in size, from a systems level of tissue organization down to sub-cellular resolution.

Herein, we present a preliminary study aimed at demonstrating the feasibility of a novel radiogenomic approach capable of extending radiology-pathology correlations to intact tissue volumes. In this study we link 3D volumetric tissue data with structural and molecular information from human prostate samples cleared using CLARITY (7) or iDISCO (8) and multi-parametric magnetic resonance imaging (mpMRI(26)).

Methods

Patients and samples

Whole mount formalin-fixed paraffin-embedded (FFPE) prostate samples from patients with prostate cancer who underwent radical prostatectomy at UCLA between May 2014 and July 2014 were obtained. Patients who had available high quality (i.e. free from artifacts and adequate for further imaging post-processing) matching pre-operative mpMRI were included for radiogenomic analysis. Thick sections of approximately 100 μm (20 times thicker than conventional histology) were cut from each sample and then cleared as described below. Adjacent thin-section (5 μm thick) hematoxylin and eosin slides (H/E) were obtained; specific regions of interest within a whole-mount were first manually delineated by the genitourinary pathologist (JH >20 years genitourinary pathology experience) and verified on both slides for histologic similarity.

Tissue clearing, staining and imaging

One sample was processed using the CLARITY procedure as previously described(7, 11). Briefly, the paraffin-embedded slide was deparaffinized, rehydrated, and then incubated with hydrogel monomer solution. The tissue-hydrogel matrices were washed with Phosphate Buffered Saline (PBS) and then incubated with sodium dodecyl phosphate (SDS) and SDS buffer. The sample was washed with PBS and incubated with primary antibodies (rabbit anti-human androgen receptor (AR), Cell Signaling, Danvers, MA), then washed with PBS and incubated with secondary antibodies (Fab fragment secondary anti-rabbit-Alexa593 antibodies, Cell Signaling, Danvers, MA). Nuclei were labeled with propidium iodide (PI) (Invitrogen, Waltham, MA). The samples were incubated with refractive index matching solution (RIMS) and then mounted on slides.

Two samples were processed with the iDISCO procedure published by Renier et al(8). Briefly, the fixed samples were first incubated with a series of methanol, bleached with

5% H2O2, and then sequentially washed in methanol, dimethyl sulfoxide (DMSO), PBS, and PBS/0.2% TritonX-100. The samples were incubated with primary antibodies (mouse anti-human alpha-methylacyl coenzyme-A racemase (AMACR), Thermo Fisher Scientific, Waltham, MA, and rabbit anti-human p63-α (p63), Cell Signaling, Danvers, MA) and with secondary antibody incubation (Cell Signaling, Danvers, MA). The samples were then washed in PTwH buffer (0.2% Tween in PBS with 10 μg/mL heparin), stained with PI (Invitrogen, Waltham, MA) and finally cleared with a simplified version of 3DISCO(10) and mounted on a chamber filled with DiBenzyl Ether (Sigma-Aldrich, St. Louis, MO). Further details on the sample processing are available in the Supplemental Methods.

Images were acquired using a Leica SP5 confocal microscope equipped with dry 10x and water-immersion 20x objectives. Imaris software (Bitplane, Concord, MA) was used for visualization. Given the clarity and relatively uniform desnity of nuclear staining, cell density estimates were performed via nuclear segmentation with Marker-controlled watershed (27) spot segmentation of nuclei as implemented in Imaris (Bitplane, Concord, MA). Seed point diameter estimates specified at different ranges (to avoid issues related to over or under segmentation as a result of variation of different size nuclei due to asynchrony of the cell cycle for the different cells) for nuclear cellular sizes from 4.5 to 6 μm in 0.25 μm increments for the nuclear stained filtered images.

MRI protocol and post-processing

All cases underwent pre-operative mpMRI on 3T systems (MAGNETOM Skyra and MAGNETOM Trio, Siemens Medical Systems) using a body array matrix and spine array coil. The standard clinical mpMRI protocol was used, including axial and coronal turbo spin-echo T2-weighted (T2w), axial echo-planar diffusion-weighted imaging (DWI), and axial dynamic contrast-enhanced MRI (DCE-MRI). Apparent diffusion coefficient (ADC; $\mu m^2/sec$), K^{trans} (influx volume transfer coefficient; min^{-1}) and and k^{ep} (outflux volume transfer coefficient; min^{-1}) were obtained from DWI and DCE-MRI data.

ADC maps were created by using the in-line post-processing software (Siemens Medical Systems) by using linear least squares curve fitting of pixels (log scale) in the four diffusion-weighted images against their corresponding b-values (0/100/400/800). The following mono-exponential decay model was used: $S = S_0 \times \exp(-b \times ADC)$, where S and S_0 are the pixel values with and without applying a b-value of diffusion sensitive gradients.

DCE-MRI images were acquired before, during, and after a single-dose injection of gadopentetate dimeglumine (Magnevist; Bayer, Wayne, NJ) at a dose of 0.1 mmol/kg through a peripheral vein at a rate of 2 mL/sec via a mechanical injector. The DCE-MRI acquisition consisted of a fast 3D RF-spoiled gradient-echo sequence, with a phase direction from left to right without fat saturation. About nine to ten unenhanced sets (total acquisition time, around 40 seconds) and approximately 65 contrast-enhanced sets of images were acquired sequentially without a delay between acquisitions. A total of 1,500 images were obtained during DCE-MRI. DCE-MRI images were evaluated by using parametric maps, processed by a separate workstation (OmniLook, iCAD, Inc., Nashua, NH). The color-coded parametric maps, K^{trans} (wash-in) and k^{ep} (wash-out), were obtained by a two-compartment

pharmacokinetic (standard Tofts) model (28). For 3D imaging, the maximum intensity projection (MIP) was applied to the manually segmented prostate.

Radiology-pathology correlations of intact prostate tissue and mpMRI

Cognitive registration was jointly performed by the pathologist and radiologist to map matched normal and tumor samples between H/E slides, cleared tissue volume samples and MRI images on the basis of zonal anatomy and identifiable imaging landmarks. AMACR staining of the 3D tissue images was assessed with binary presence/absence determinations by the pathologist (JH). Segmented cell counts were performed on the cleared tissue images throughout the sampled regions in a voxel-wise basis using the Imaris software (Bitplane, Concord, MA). T-test calculations were performed for cellular density, ADC and K^{trans} comparisons between tumor and normal tissue areas with significance criteria $p < 0.05$. If the F-test for variance equality was significantly different between the measurements then Welch's t-test was used, otherwise Student's t-test was used. The measured quantities were plotted as box plots with the interquartile (IQR) percentage and whiskers at +/−1.5*IQR.

Results

Patients and samples

This study involved retrospective analysis according to an institutional review board–approved, Health Insurance Portability and Accountability Act protocol permitting evaluation of resected tissue specimens and diagnostic imaging studies. Five patients with prostate cancer and available whole-mount prostate samples suitable for tissue clearing with matching pre-operative multi-parametric MR images were identified. Two patients were excluded due to inadequate quality of the pre-operative MR studies. The mean age of the remaining patients was 59 ± 9 years; Patients 1 and 2 had unifocal Gleason 4+3 prostate cancer and Patient 3 had a multifocal prostate cancer (Gleason 4+3, 3+3, and 3+3).

Tissue clearing, staining and imaging

All three samples were successfully cleared, stained and visualized using either CLARITY or iDISCO. Our first goal was to establish the feasibility of implementing CLARITY with FFPE whole mount prostate glands. We selected a thick-section (100 um) of non-tumor, normal glandular tissue from the whole mount gland in the first patient (Patient 1), a 55 year-old male with a unifocal Gleason 4 + 3 prostate cancer. Applying CLARITY, we were able to clear the tissue and make it optically transparent with minimal tissue distortion (<10%/unit area) no significant tissue loss (Figure 1a). The sample was subsequently double stained with anti-AR antibodies and the nuclear dye and then imaged at 10x, revealing good fluorescent signal uniformly present throughout the thickness of the sample from both AR stained cells and stained nuclei as well as good preservation and visualization of prostate glandular structures (Fig 1b, S1, S2). The same matched areas of the whole mount imaged with CLARITY and with conventional microscopy (on the adjacent H/E slide) revealed comparable glandular appearance, typical of normal prostate (Fig 1b).

Next, we applied the alternative solvent-based iDISCO method on the second sample (Patient 2), a 53 year-old male with unifocal Gleason 4+3 prostate cancer. We similarly

selected a thick-section (100 um) whole mount sample of non-tumor, normal glandular tissue from the whole mount gland. iDISCO was also able to clear the thick section normal prostate glandular tissue without apparent tissue loss or distortion (Fig 2). The sample was then double stained with the basal cell-specific anti-p63 antibody (29, 30) and the nuclear dye. Homogenous signal was detected from both the anti-p63 antibody and the nuclear dye throughout the entire thickness of the specimen. Again, normal glandular structures were clearly identifiable and similar in appearance compared to the adjacent H/E thin slide, without architectural distortion (Fig 2b, Fig S3). Compared to CLARITY, iDISCO provided a higher signal-to-noise ratio, while total sample processing was twice as fast (2 weeks versus 5.5 weeks).

Based on these initial results we used iDISCO for processing the tissue from the third sample (Patient 3), a 69 year-old patient with multifocal prostate cancer (Gleason 4+3, 3+3, 3+3 for the three foci, respectively). This time our goal was to evaluate tumor regions in the whole mount gland, we therefore selected a tissue volume (100 μm) containing both cancer and non-cancer areas in the same sample. After applying the immunofluorescent antibody against AMACR, a known tissue marker of prostate cancer (31-33), and the nuclear staining, the processed sample was imaged using 10x (Fig 3b) and 20x (Fig 3c, Fig S4) lenses. The image quality and the fluorescent signal were overall comparable to the previous iDISCO sample (Fig 3, S4). Differences in tissue architecture were evident in both low- and high-power images between normal and tumor areas (Fig 3b, c), with similar tissue characteristics to the matched regions on the adjacent H/E slide.

Radiology-pathology correlations of intact prostate tissue and mpMRI

Having established our ability to clear thick section prostate samples, and to apply both intrinsic and immune-labeled stains, we next performed a two-step analysis first descriptively comparing quantitative mpMRI parameters, including ADC and K^{trans}, to the qualitative intact tissue characteristics of the matched prostate samples after clearing in all three patients, and then quantitatively correlating mpMRI parameters with automatically extracted cell count data from normal and tumor areas for Patient 3. For Patients 1 and 2, high ADC and low K^{trans} values and T2W signal iso-intensity were registered in the normal gland areas imaged on the cleared thick sections (Fig 1c, Fig 2c), which were consistent with mpMRI features of normal prostate (34-39). The microscopic appearance and architecture of the gland and presence, distribution and gross quantity of nuclear, p63 and AR staining in the matching regions on the cleared volume samples (confirmed by pathological analysis) were consistent with normal prostate glandular tissue and consistent with expected findings from the H/E slides of normal prostate glands for patients 1 and 2.

We next performed a quantitative analysis comparing normal and tumor tissue regions in Patient 3. mpMRI maps relative to a portion of the main tumor focus (Gleason 4+3, Fig 3d) showed statistically significant differences between normal and cancer tissue (ADC= 826.8 +/− 89.9 vs. 1 839.2 +/− 67.0 μm^2/sec, $p=8.57 \times 10^{-15}$ by Student's t-test and K^{trans} = 0.358 +/− 0.083 vs. 0.138 +/−0.011 min^{-1}, $p=3.81 \times 10^{-5}$ by Welch's t-test, Fig 4c), indicative of differences in higher cell density and tissue perfusion consistent with typical features of prostate cancer (34-39). 3D volume images of the cleared tissue reflected the

regional differences observed by mpMRI with significantly increased cellular density (6 353+/− 923 cells/μm^3 vs. 4401 +/− 924 cells/μm^3, p=0.0019 by Student's t-test) as well as positive AMACR staining in the tumor region relative to the adjacent normal region (Fig 3, 4). Quantitative analysis revealed a statistically significant difference in cell density between normal and tumor areas on the cleared sample (p=0.0019, Fig 4c), consistent with the differences in ADC and K^{trans} between the same matched normal and tumor areas (3D MIP imaging of T2-weighted MRI, ADC maps and K^{trans} maps for Patient 3 are available in the Supplemental Material).

Discussion

In this study, we demonstrate the feasibility of complete tissue clearing and subsequent cellular and molecular phenotyping of whole mount prostate samples twenty times thicker than traditional histology using CLARITY (7) and iDISCO (8) in normal and cancer specimens. We then show that quantitative and qualitative mpMRI features reflect the features seen on the cleared intact prostate volumes as well as traditional H/E thin sections. Finally, quantitative analysis of cellular count data from the cleared tissue volumes revealed significant differences between normal and tumor areas, which were mirrored by differences in K^{trans} and ADC.

These initial results show the validity and usefulness of tissue clearing for the 3D microscopic imaging of human prostate and the potential impact of applying them as a tool for the advancement of the radiology-pathology correlation assessment. In this setting, the recent developments in tissue clearing technologies present now the opportunity to obtain a highly resolved radiogenomic map of spatially preserved structural, molecular, and functional information from intact tissue specimens. Compared to a traditional two-dimensional-based approach, a volume-based analysis allows for improved phenotypic-genotypic understanding of spatial relationships capable of spanning many orders of magnitude and can potentially be applied to almost any clinical imaging setting in which imaging-tissue correlation is possible. The advantages of this new radiogenomic approach however, extend beyond the simple possibility to more precisely analyze and correlate 3D structures seen by imaging. The compatibility of next-generation clearing techniques with immunofluorescent labeling also allows one to generate detailed in-situ three dimensional molecular portrayals of cells, organelles, peptides and even nucleic acids on the same samples while preserving their spatial arrangements (40, 41). Multiple rounds of molecular labeling are also possible on the same tissue volume increasing the number of structures that can be targeted, which is not possible with current immunohistochemical techniques (7, 40). Volume-based radiogenomic analysis thus potentially provides a crucial missing link between 3D structural and functional observations captured with noninvasive imaging, and the actual topography of constituent tissue structures, cancer cells and their local microenvironment, allowing direct visualization of intratumoral heterogeneity across the intact tumor volume (42-44). As new methods and variations are developed, we expect further improvements in technical and efficiency of tissue clearing (4). For example during the period of time with our samples, the development of iDISCO provided a significant advantage in processing time over CLARITY. Additionally the transient tissue expansion

that may occur with CLARITY is not seen in IDISCO, to the contrary there is a small amount of shrinkage (5).

The small sample size (three patients and a single cancer sample) is clearly a limitation that necessitates future studies involving larger cohorts, ideally prospectively, in a manner that allows more comprehensive evaluation of specificty and sensitivity, before being applied in a clinical context. Thus, these results are presented as an initial study demonstrating the feasibility and potential utility of approach and measurements. Additionally, there are limitations inherent to the currently available tissue clearing technologies, complicating the achievement of complete 3D imaging of very large-volume tissues, including long sample processing and imaging times, relatively limited depth of antibody penetration through the sample, and the non-trivial cost. Further limitations of this study lie in the small thickness of the samples relative to the larger thickness of the MRI slices, as well as the small number of specimens and antigens evaluated. However there continues to be technical advancement enabling shorter tissue processing times as well as deeper penetration of tissues allowing for larger specimens, thus in the foreseeable future this approach can be applied to larger volumes, different tissue types, molecular stains and different computational approaches for mapping and registration, with a potential to significantly impact the diagnostic characterization of tissue specimens.

Conclusion

In summary, we demonstrate the feasibility of a novel integrative imaging approach that enables 3D spatially preserved correlations across multiple spatial scales. This could have enormous impact upon multiple dimensions of investigation including but not limited to improving understanding of histopathology and radiology correlates of normal and diseased tissues, as well as providing a powerful means to better understand cellular and genomic spatial heterogeneity.

Supplementary Material

Refer to Web version on PubMed Central for supplementary material.

Funding

NJ was supported by the Prostate Cancer Foundation (the Stewart Rahr–PCF Young Investigator Award) and a NIH NCATS and NIBIB UCLA CTSI Grant Number KL2TR001882 (PD: Wong). MDK and NJ were supported by UCLA Prostate Cancer Spore Career Development Award (NCI SPORE 2P50CA092131).

Abbreviations:

H/E

AR

AMACR

PI

FFPE

ADC

mpMRI

SDS

RIMS

DMSO

PBS

REFERENCES

1. Insel TR, Young LJ. The neurobiology of attachment. Nature reviews Neuroscience. 2001;2(2):129–36. [PubMed: 11252992]
2. Mombaerts P, Wang F, Dulac C, Chao SK, Nemes A, Mendelsohn M, et al. Visualizing an olfactory sensory map. Cell. 1996;87(4):675–86. [PubMed: 8929536]
3. Richardson DS, Lichtman JW. Clarifying Tissue Clearing. Cell. 2015;162(2):246–57. [PubMed: 26186186]
4. Azaripour A, Lagerweij T, Scharfbillig C, Jadczak AE, Willershausen B, Van Noorden CJ. A survey of clearing techniques for 3D imaging of tissues with special reference to connective tissue. Prog Histochem Cytochem. 2016;51(2):9–23. [PubMed: 27142295]
5. Yu T, Qi Y, Gong H, Luo Q, Zhu D. Optical clearing for multiscale biological tissues. J Biophotonics. 2018;11(2).
6. Spalteholz W. Uber das Durchsichtigmachen von menschlichen und tierischen Praparaten und seine theoretischen Bedingungen, nebst Anhang: Uber Knochenfarbung. Leipzig: S. Hirzel; 1914.
7. Chung K, Wallace J, Kim SY, Kalyanasundaram S, Andalman AS, Davidson TJ, et al. Structural and molecular interrogation of intact biological systems. Nature. 2013;497(7449):332–7. [PubMed: 23575631]
8. Renier N, Wu Z, Simon DJ, Yang J, Ariel P, Tessier-Lavigne M. iDISCO: a simple, rapid method to immunolabel large tissue samples for volume imaging. Cell. 2014;159(4):896–910. [PubMed: 25417164]
9. Dodt H-U, Leischner U, Schierloh A, Jahrling N, Mauch CP, Deininger K, et al. Ultramicroscopy: three-dimensional visualization of neuronal networks in the whole mouse brain. Nat Meth. 2007;4(4):331–6.
10. Erturk A, Lafkas D, Chalouni C. Imaging cleared intact biological systems at a cellular level by 3DISCO. Journal of visualized experiments : JoVE. 2014(89).
11. Tomer R, Ye L, Hsueh B, Deisseroth K. Advanced CLARITY for rapid and high-resolution imaging of intact tissues. Nature protocols. 2014;9(7):1682–97. [PubMed: 24945384]
12. Yang B, Treweek JB, Kulkarni RP, Deverman BE, Chen CK, Lubeck E, et al. Single-cell phenotyping within transparent intact tissue through whole-body clearing. Cell. 2014;158(4):945–58. [PubMed: 25088144]
13. Kuwajima T, Sitko AA, Bhansali P, Jurgens C, Guido W, Mason C. ClearT: a detergent- and solvent-free clearing method for neuronal and non-neuronal tissue. Development. 2013;140(6):1364–8. [PubMed: 23444362]
14. Hua L, Zhou R, Thirumalai D, Berne BJ. Urea denaturation by stronger dispersion interactions with proteins than water implies a 2-stage unfolding. Proceedings of the National Academy of Sciences of the United States of America. 2008;105(44):16928–33. [PubMed: 18957546]
15. Susaki EA, Tainaka K, Perrin D, Kishino F, Tawara T, Watanabe TM, et al. Whole-brain imaging with single-cell resolution using chemical cocktails and computational analysis. Cell. 2014;157(3):726–39. [PubMed: 24746791]

16. Murphey MD, Madewell JE, Olmsted WW, Ros PR, Neiman HL. A history of radiologic pathology correlation at the Armed Forces Institute of Pathology and its evolution into the American Institute for Radiologic Pathology. Radiology. 2012;262(2):623–34. [PubMed: 22187632]

17. Diehn M, Nardini C, Wang DS, McGovern S, Jayaraman M, Liang Y, et al. Identification of noninvasive imaging surrogates for brain tumor gene-expression modules. Proceedings of the National Academy of Sciences of the United States of America. 2008;105(13):5213–8. [PubMed: 18362333]

18. Segal E, Sirlin CB, Ooi C, Adler AS, Gollub J, Chen X, et al. Decoding global gene expression programs in liver cancer by noninvasive imaging. Nature biotechnology. 2007;25(6):675–80.

19. Yamamoto S, Huang D, Du L, Korn RL, Jamshidi N, Burnette BL, et al. Radiogenomic Analysis Demonstrates Associations between (18)F-Fluoro-2-Deoxyglucose PET, Prognosis, and Epithelial-Mesenchymal Transition in Non-Small Cell Lung Cancer. Radiology. 2016;280(1):261–70. [PubMed: 27082783]

20. Jamshidi N, Jonasch E, Zapala M, Korn RL, Brooks JD, Ljungberg B, et al. The radiogenomic risk score stratifies outcomes in a renal cell cancer phase 2 clinical trial. European radiology. 2016;26(8):2798–807. [PubMed: 26560727]

21. Yamamoto S, Han W, Kim Y, Du L, Jamshidi N, Huang D, et al. Breast Cancer: Radiogenomic Biomarker Reveals Associations among Dynamic Contrast-enhanced MR Imaging, Long Noncoding RNA, and Metastasis. Radiology. 2015;275(2):384–92. [PubMed: 25734557]

22. Jamshidi N, Jonasch E, Zapala M, Korn RL, Aganovic L, Zhao H, et al. The Radiogenomic Risk Score: Construction of a Prognostic Quantitative, Noninvasive Image-based Molecular Assay for Renal Cell Carcinoma. Radiology. 2015;277(1):114–23. [PubMed: 26402495]

23. Yamamoto S, Korn RL, Oklu R, Migdal C, Gotway MB, Weiss GJ, et al. ALK molecular phenotype in non-small cell lung cancer: CT radiogenomic characterization. Radiology. 2014;272(2):568–76. [PubMed: 24885982]

24. Jamshidi N, Diehn M, Bredel M, Kuo MD. Illuminating radiogenomic characteristics of glioblastoma multiforme through integration of MR imaging, messenger RNA expression, and DNA copy number variation. Radiology. 2014;270(1):1–2.

25. Yamamoto S, Maki DD, Korn RL, Kuo MD. Radiogenomic analysis of breast cancer using MRI: a preliminary study to define the landscape. AJR Am J Roentgenol. 2012;199(3):654–63. [PubMed: 22915408]

26. Langer DL, vd Kwast TH, Evans AJ, Plotkin A, Trachtenberg J, Wilson BC, et al. Prostate Tissue Composition and MR Measurements: Investigating the Relationships between ADC, T2, Ktrans, ve, and Corresponding Histologic Features. Radiology. 2010;255(2):485–94. [PubMed: 20413761]

27. Meyer F, Beucher S. The Morphological Approach to Segmentation: The Watershed Transformation. Mathematical Morphology in Image Processing: CRC Press; 1993. p. 49.

28. Tofts PS. Modeling tracer kinetics in dynamic Gd-DTPA MR imaging. Journal of magnetic resonance imaging : JMRI. 1997;7(1):91–101. [PubMed: 9039598]

29. Signoretti S, Waltregny D, Dilks J, Isaac B, Lin D, Garraway L, et al. p63 Is a Prostate Basal Cell Marker and Is Required for Prostate Development. The American Journal of Pathology. 2000;157(6):1769–75. [PubMed: 11106548]

30. Zhou M, Shah R, Shen R, Rubin MA. Basal cell cocktail (34betaE12 + p63) improves the detection of prostate basal cells. The American journal of surgical pathology. 2003;27(3):365–71. [PubMed: 12604893]

31. Xu J, Stolk JA, Zhang X, Silva SJ, Houghton RL, Matsumura M, et al. Identification of Differentially Expressed Genes in Human Prostate Cancer Using Subtraction and Microarray. Cancer Research. 2000;60(6):1677. [PubMed: 10749139]

32. Welsh JB, Sapinoso LM, Su AI, Kern SG, Wang-Rodriguez J, Moskaluk CA, et al. Analysis of Gene Expression Identifies Candidate Markers and Pharmacological Targets in Prostate Cancer. Cancer Research. 2001;61(16):5974. [PubMed: 11507037]

33. Rubin MA, Zhou M, Dhanasekaran SM, Varambally S, Barrette TR, Sanda MG, et al. alpha-Methylacyl coenzyme A racemase as a tissue biomarker for prostate cancer. Jama. 2002;287(13):1662–70. [PubMed: 11926890]

34. Padhani AR, Gapinski CJ, Macvicar DA, Parker GJ, Suckling J, Revell PB, et al. Dynamic contrast enhanced MRI of prostate cancer: correlation with morphology and tumour stage, histological grade and PSA. Clinical radiology. 2000;55(2):99–109. [PubMed: 10657154]
35. Rouviere O, Raudrant A, Ecochard R, Colin-Pangaud C, Pasquiou C, Bouvier R, et al. Characterization of time-enhancement curves of benign and malignant prostate tissue at dynamic MR imaging. European radiology. 2003;13(5):931–42. [PubMed: 12695812]
36. Xu J, Humphrey PA, Kibel AS, Snyder AZ, Narra VR, Ackerman JJ, et al. Magnetic resonance diffusion characteristics of histologically defined prostate cancer in humans. Magnetic resonance in medicine. 2009;61(4):842–50. [PubMed: 19215051]
37. Rosenkrantz AB, Sigmund EE, Johnson G, Babb JS, Mussi TC, Melamed J, et al. Prostate cancer: feasibility and preliminary experience of a diffusional kurtosis model for detection and assessment of aggressiveness of peripheral zone cancer. Radiology. 2012;264(1):126–35. [PubMed: 22550312]
38. Vos EK, Litjens GJ, Kobus T, Hambrock T, Hulsbergen-van de Kaa CA, Barentsz JO, et al. Assessment of prostate cancer aggressiveness using dynamic contrast-enhanced magnetic resonance imaging at 3 T. European urology. 2013;64(3):448–55. [PubMed: 23751135]
39. Rothke M, Blondin D, Schlemmer HP, Franiel T. [PI-RADS classification: structured reporting for MRI of the prostate]. RoFo : Fortschritte auf dem Gebiete der Rontgenstrahlen und der Nuklearmedizin. 2013;185(3):253–61. [PubMed: 23404430]
40. Murray E, Cho JH, Goodwin D, Ku T, Swaney J, Kim SY, et al. Simple, Scalable Proteomic Imaging for High-Dimensional Profiling of Intact Systems. Cell. 2015;163(6):1500–14. [PubMed: 26638076]
41. Sylwestrak Emily L, Rajasethupathy P, Wright Matthew A, Jaffe A, Deisseroth K. Multiplexed Intact-Tissue Transcriptional Analysis at Cellular Resolution. Cell.164(4):792–804. [PubMed: 26871636]
42. Gerlinger M, Rowan AJ, Horswell S, Larkin J, Endesfelder D, Gronroos E, et al. Intratumor heterogeneity and branched evolution revealed by multiregion sequencing. N Engl J Med. 2012;366(10):883–92. [PubMed: 22397650]
43. Gerlinger M, Swanton C. How Darwinian models inform therapeutic failure initiated by clonal heterogeneity in cancer medicine. Br J Cancer. 2010;103(8):1139–43. [PubMed: 20877357]
44. Navin N, Kendall J, Troge J, Andrews P, Rodgers L, McIndoo J, et al. Tumour evolution inferred by single-cell sequencing. Nature. 2011;472(7341):90–4. [PubMed: 21399628]

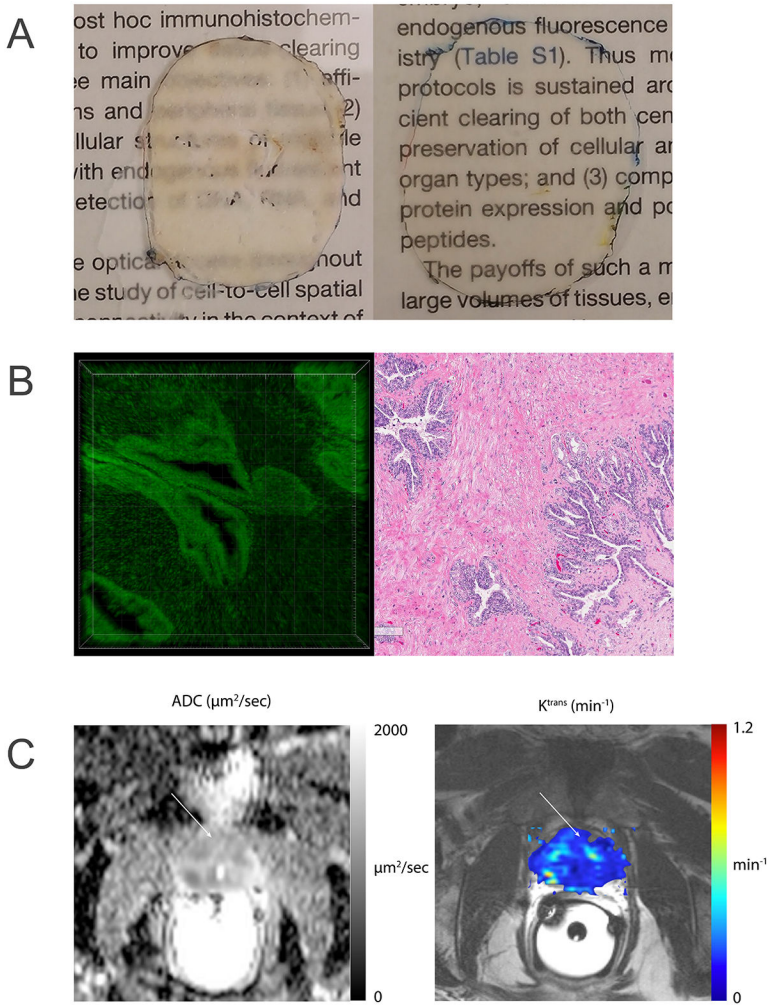

Figure 1. CLARITY sample processing and normal tissue imaging

Patient 1 is a 55 year-old male with Gleason 4+3 prostate cancer. (a) Whole mount 100 μm thick section before (left) and after (right) clearing with CLARITY. (b) Normal glandular structures from the same area are shown in the volumetric confocal images (left) and on the adjacent thin section H/E slide (right), revealing similar architectural features. The green signal in the CLARITY image is the fluorescently labeled antibody anti-AR. (c) Multiparametric-MRI with ADC (left) and K^{trans} (right) maps. The white arrows point at the areas shown in (b), ADC and K^{trans} values in these areas are suggestive of normal prostate tissue. In contrast, the red arrows indicate regions of low ADC and high K^{trans} in the right posterior aspect of the gland, corresponding to Gleason 4+3 prostate cancer nodules. The ADC and K^{trans} color codes appear along the right-most column, corresponding to black and white 0-2000 μ^2/sec and rainbow 0-1.2 min^{-1}, respectively. Scale bars are 100 microns.

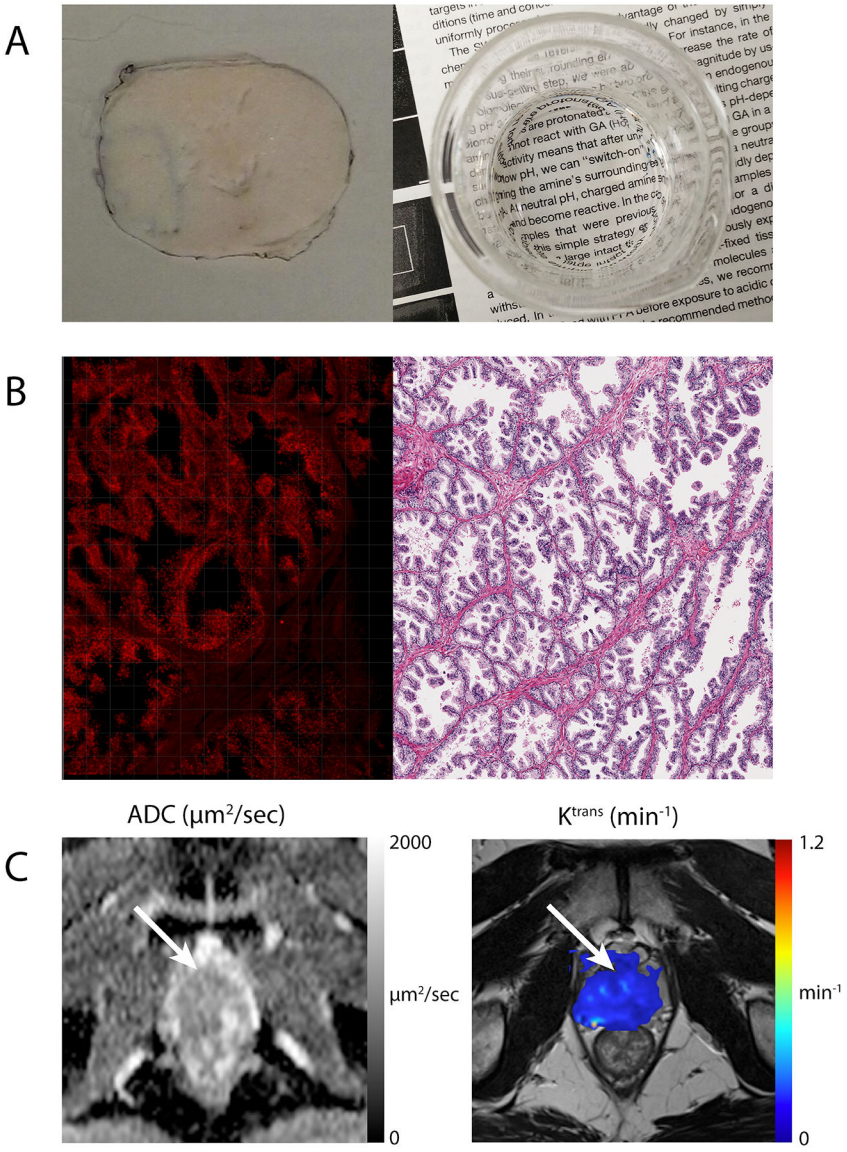

Figure 2. iDISCO sample processing and normal tissue imaging

Patient 2 is a 53 year-old male with Gleason 4+3 prostate cancer. (a) Whole mount 100 μm thick section before (left) and after (right) clearing using iDISCO. (b) Normal prostate glands from the same prostate area are shown on the thick iDISCO-processed section (left) and on the adjacent H/E slide (right). Similarities in tissue architecture are evident between the two techniques. The red signal from the volume images is the antibody anti-p63. (c) mpMRI images showing ADC (left) and K^{trans} (right) maps. The white arrows point in the ADC and K^{trans} correspond to the histological regions in (b), reflecting concordance between histology and mpMR for normal prostate. Scale bars are 100 microns.

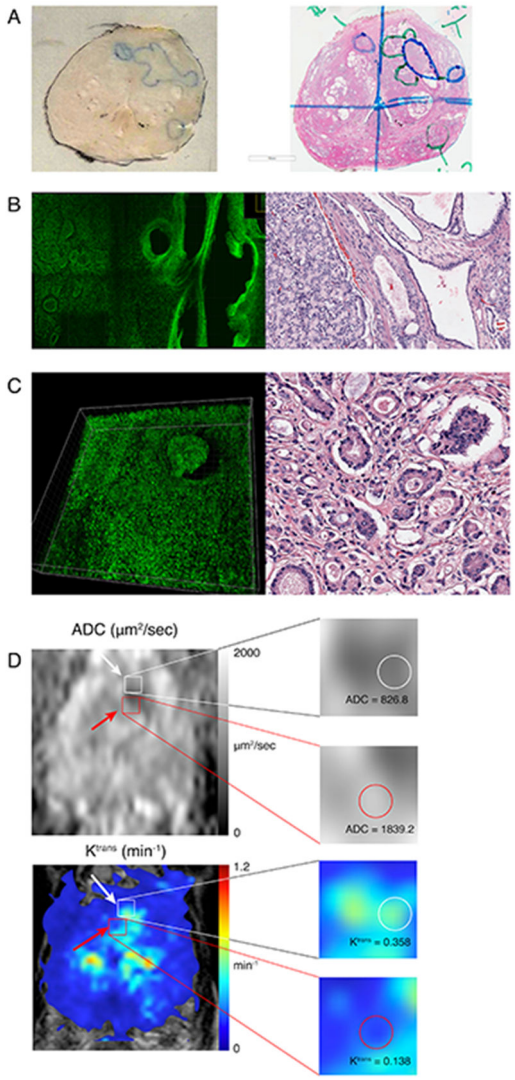

Figure 3. iDISCO sample showing regional architectural differences in normal vs. tumor areas and correlations with mpMRI

Patient 3 is a 69 year-old male with multifocal prostate cancer. (a) Whole mount 100um-thick prostate sample before iDISCO processing (left) and corresponding adjacent H/E thin section (right). (b) Low power (10x) images of both the iDISCO volume sample (left) and the thin H/E slide (right) showing a transition area between normal tissue (on the right of the field of view) and tumor (on the left of the field of view). (c) High power (20x) images of a tumor area on the iDISCO (left) and H/E (right) samples. The green signal on the iDISCO image is the antibody anti-AMACR. Both the H/E and the cleared tissue volume images show similar tissue organization and cellular density. (d) mpMR images with ADC (top) and K^{trans} (bottom) maps. The white and red arrows indicate prostate cancer and normal tissue, respectively. The zoomed-in multi-parametric maps show clear differences between prostate cancer and normal tissue (ADC = 826.8 vs. 1 839.2 and K^{trans} = 0.358 vs. 0.138), indicative of differences in higher cell density and tissue perfusion, consistent with typical imaging features of prostate cancer. The ADC and K^{trans} color codes appear along

the rightmost column, corresponding to black and white 0-2000 μ^2/sec and rainbow 0-1.2 min^{-1}, respectively. Scale bars are 100 microns.

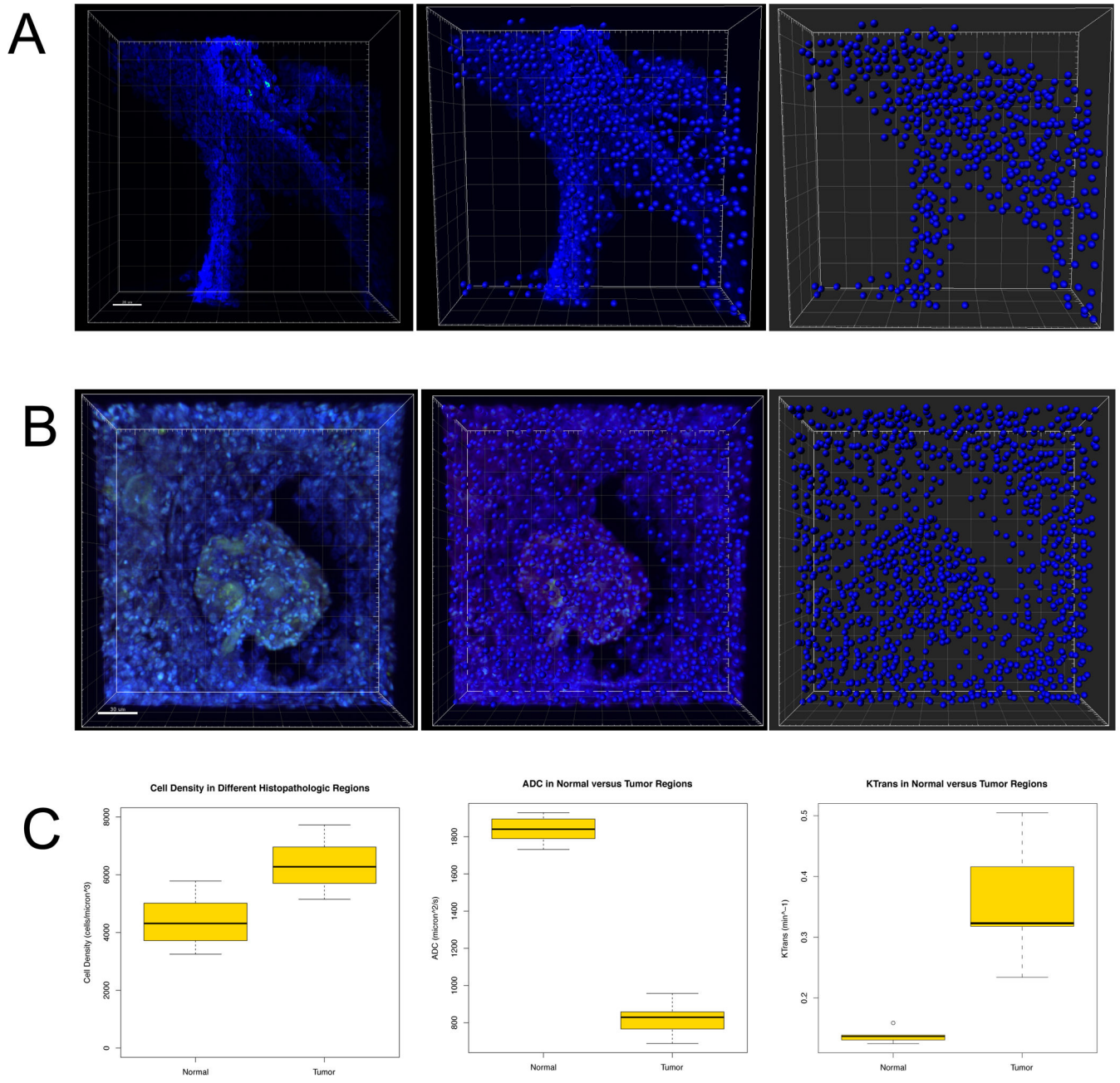

Figure 4. Quantitative analysis of normal vs tumor areas in Patient 3

Normal prostate glands (a) and a tumor area (b) with a mass infiltrating a glandular duct from Patient 3 are shown. The left panels in (a) and (b) reveal differences in AMACR (green) signal. The central panels in (a) and (b) show both the fluorescent signal and the segmented nuclei, while the right panels only show the segmented nuclei. (c) Boxplot showing significantly different cellular densities in the normal vs. tumor areas (left, p=0.0019, Student's t-test, F=1). The central and right panels in (c) show differences in terms of ADC ($p=8.57 \times 10^{-15}$, Student's t-test, F=0.6) and K^{trans} ($p=3.81 \times 10^{-5}$, Welch's

t-test, F=0.02) in the corresponding matched normal and tumor areas. Scale bars are 30 microns.